UC Davis
UC Davis Previously Published Works

Title

Comparison of the Forward and Reverse Photocycle Dynamics of Two Highly Similar Canonical Red/Green Cyanobacteriochromes Reveals Unexpected Differences

Permalink

Journal

ISSN

Authors

Kirpich, Julia S
Chang, Che-Wei
Franse, Jasper
et al.

Publication Date

DOI

Peer reviewed

Comparison of the Forward and Reverse Photocycle Dynamics of Two Highly Similar Canonical Red/Green Cyanobacteriochromes Reveals Unexpected Differences

Julia S. Kirpich, Che-Wei Chang, Jasper Franse, Qinhong Yu, Francisco Velazquez Escobar, Adam J. Jenkins, Shelley S. Martin, Rei Narikawa, James B. Ames, J. Clark Lagarias, and Delmar S. Larsen*

Read Online

ACCESS | Metrics & More | Article Recommendations | Supporting Information

ABSTRACT: Cyanobacteriochromes (CBCRs) are cyanobacterial photoreceptors that exhibit photochromism between two states: a thermally stable dark-adapted state and a metastable light-adapted state with bound linear tetrapyrrole (bilin) chromophores possessing 15Z and 15E configurations, respectively. The photodynamics of canonical red/green CBCRs have been extensively studied; however, the time scales of their excited-state lifetimes and subsequent ground-state evolution rates widely differ and, at present, remain difficult to predict. Here, we compare the photodynamics of two closely related red/green CBCRs that have substantial sequence identity (∼68%) and similar chromophore environments: AnPixJg2 from *Anabaena* sp. PCC 7120 and NpR6012g4 from *Nostoc punctiforme*. Using broadband transient absorption spectroscopy on the primary (125 fs to 7 ns) and secondary (7 ns to 10 ms) time scales together with global analysis modeling, our studies revealed that AnPixJg2 and NpR6012g4 have comparable quantum yields for initiating the forward ($^{15Z}P_r \rightarrow {}^{15E}P_g$) and reverse ($^{15E}P_g \rightarrow {}^{15Z}P_r$) reactions, which proceed through monotonic and nonmonotonic mechanisms, respectively. In addition to small discrepancies in the kinetics, the secondary reverse dynamics resolved unique features for each domain: intermediate shunts in NpR6012g4 and a Meta-G_f intermediate red-shifted from the $^{15Z}P_r$ photoproduct in AnPixJg2. Overall, this study supports the conclusion that sequence similarity is a useful criterion for predicting pathways of the light-induced evolution and quantum yield of generating primary intermediate Φ_p within subfamilies of CBCRs, but more studies are still needed to develop a comprehensive molecular level understanding of these processes.
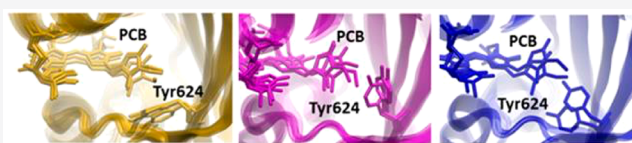
Phytochromes are red/far-red photosensory proteins that utilize the photoisomerization of linear tetrapyrrole (bilin) chromophores to detect the ratio of red to far-red light.[2] Cyanobacteriochromes (CBCRs) are distantly related photosensors that also bind bilins but exhibit a spectral range that is greater than that of phytochromes.[3−10] Like phytochromes, CBCRs respond to light via isomerization of the C15=C16 bond of their embedded bilin chromophores as depicted for CBCRs with red/green photocycles (Figure 1). Light absorption initiates D-ring rotation on a picosecond time scale with subsequent structural transformations of the surrounding GAF (cGMP phosphodiesterase/adenylyl cyclase/FhlA) protein scaffold that accompany reversible conversion of the dark-adapted (15Z) and metastable (15E) light-activated "photoproduct" states. Isolated CBCR GAF domains are sufficient for reversible photochemistry, although CBCR GAF domains are often found in tandem in the full-length protein context. On the basis of their diverse spectral sensitivities, CBCRs have been categorized into multiple families corresponding to their reversible photocycles. These include the canonical red/green,[4,8,11] green/red,[12−14] insert-cysteine,[7] DXCF,[3,7,9] and multiple far-red/red and far-red orange families.[10,15−19]

Canonical red/green CBCRs have been extensively studied by ultrafast (femtoseconds to nanoseconds)[20−25] and long time (nanoseconds to milliseconds)[11,24,26−28] spectroscopies. However, the molecular basis for differences in red/green CBCR excited-state lifetimes and time scales of the primary Lumi photointermediate formation in the forward direction[20] is unresolved. On the basis of primary dynamics differences, three classes of canonical red/green CBCRs have been distinguished. Class I$_F$ red/green CBCRs (NpF2164g5, B2J668; and NpR1597g4, B2J0R5) are fluorescent and show no resolvable photointermediate within the first few nanoseconds. Class II$_F$ CBCRs (NpR5113g2, B2J261; NpF2164g6, B2J668; and NpR6012g4, B2IU14) generate transient red-shifted Lumi-R$_f$ photointermediates that evolve to a stable $^{15E}P_g$ photoproduct.
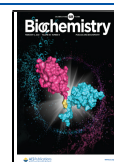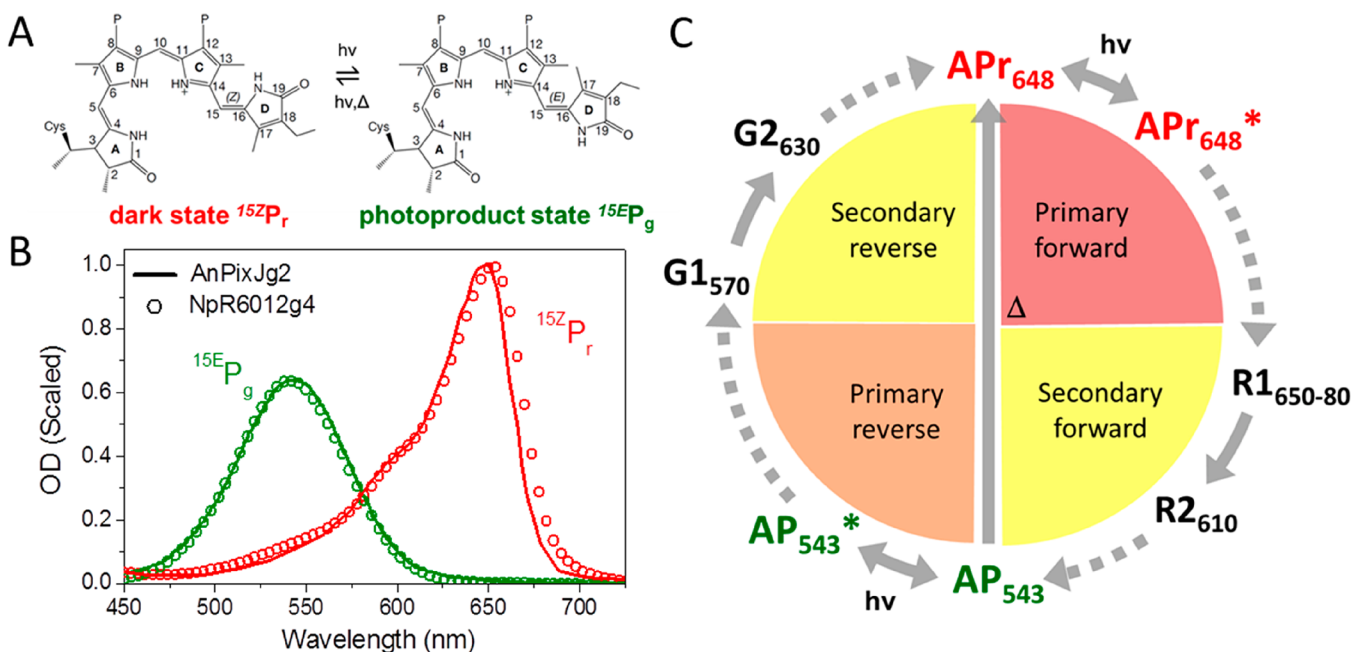
Figure 1. (A) Molecular structure of phycocyanobilin (PCB) in both the $^{15Z}P_r$ state (left) and the $^{15E}P_g$ state (right). (B) Ground-state absorption spectra of AnPixJg2 [λ_{max} = 648 and 543 nm (solid curves)] compared with those of NpR6012g4 [λ_{max} = 651 and 540 nm (empty circles)]. $^{15Z}P_r$ spectra (red) are normalized at their respective maximum absorption wavelengths. $^{15E}P_g$ spectra (green) are scaled to their respective $^{15Z}P_r$ spectra. (C) Photocycle scheme of a representative canonical red/green CBCR.[26] Curvy solid gray arrows indicate the direction of the reaction propagation from one state to another, and curvy dotted gray arrows the reaction propagation direction with the possibility of the presence of the photointermediates other than those listed in the scheme. The straight gray arrow in the middle indicates dark reversion.

Class III$_F$ CBCRs (NpAF142g2, B2JAQ4; NpR4776g3, B2IZ18; NpF2854g3, B2IVK2; and NpF2164g4, B2J668) yield Lumi-R$_f$ photointermediates that yield blue-shifted Meta-R$_y$ intermediates on a nanosecond time scale prior to stable photoproduct formation. For this class, Meta-R$_y$ was the first of several subsequent blue-shifted intermediates that were associated with stepwise structural deformation of the chromophore.[29,30] In some cases, secondary forward dynamics analyses of the red/green CBCRs also resolved a nonproductive $^{15Z}P_o$ subpopulation that generated a Lumi-O$_f$ photointermediate that decayed back to the ground state.[29,30] As with primary forward dynamics investigations, the primary reverse dynamics of several red/green CBCRs resolved three classes. Class I$_R$ (NpF2164g6) resolved only a red-shifted Lumi-G$_o$ intermediate. Both of the remaining classes resolved Lumi-G$_o$ intermediates that more rapidly evolved to secondary intermediates. Class II$_R$ (NpAF142g2, NpF2164g4, NpF2854g3, and NpR6012g4) resolved blue-shifted Meta-G$_y$ intermediates, whereas class III$_R$ (NpR1597g4, NpR4776g3, and NpR5113g2) resolved red-shifted Meta-G$_r$ intermediates on the nanosecond time scale.[31]

This study was undertaken to compare the static properties and dynamic photoactivity of the GAF2 photosensory domain of the AnPixJ cyanobacteriochrome (AnPixJg2) from *Anabaena* sp. PCC 7120 and GAF4 of the NpR6012 cyanobacteriochrome (NpR6012g4) from *Nostoc punctiforme*, two red/green CBCRs that share ~68% sequence identity (Figure S1). Despite their similarity, the two CBCRs are found in quite different protein architectures in their full-length protein context (Scheme 1). Previously, NpR6012g4 has been studied with static spectroscopic techniques in the ultraviolet−visible range along with mutational analysis,[8,32,33] by multipulse ultrafast spectroscopy,[20−23,34] and by solution-phase nuclear magnetic resonance

Scheme 1. Domain Architectures of AnPixJ and NpR6012[a]
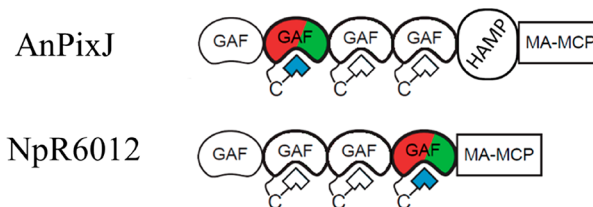
[a]The two GAF domains investigated here are highlighted with colors to represent their red-absorbing $^{15Z}P_r$ and green-absorbing $^{15E}P_g$ states. Legend: GAF, domain name representing cGMP phosphodiesterase/adenylyl cyclase/FhlA families; MA-MCP, methyl-accepting chemotaxis protein output domain; HAMP, domain name representing histidine kinases, adenylate cyclases, methyl-accepting proteins, and phosphatases. The chromophore is colored blue for aesthetic purposes only.

(NMR).[35,36] AnPixJg2 has been explored by static optical, infrared (IR), and resonance Raman spectroscopy,[26,27,37,38] X-ray crystallography,[39,40] solid-state NMR approaches,[38,41] molecular dynamics (MD) simulations,[42] and transient electronic spectroscopy.[26] To date, the ultrafast forward and reverse photodynamics have not been reported for AnPixJg2 and the secondary reverse dynamics have not been reported for NpR6012g4. We report them here. This study compares the primary photodynamics and previously published secondary forward ($^{15Z}P_r \rightarrow {}^{15E}P_g$) and reverse ($^{15E}P_g \rightarrow {}^{15Z}P_r$) reaction dynamics of AnPixJg2 with those of NpR6012g4.[21−23,30] These studies seek to provide comparative insight into two highly related canonical red/green CBCRs compared with those more diverged analyzed previously.[20,25,29]

◼ MATERIALS AND METHODS

Sample Preparation. AnPixJg2 and NpR6012g4 were expressed as previously described.[7] Static absorption spectra of AnPixJg2 in the dark-adapted $^{15Z}P_r$ and light-adapted $^{15E}P_g$ states were acquired at 25 °C on a modified Cary 50 instrument with saturating top-down illumination of the sample using a filtered xenon source.[43] Bandpass filters of 650 ± 20 and 500 ± 20 nm were used to trigger forward and reverse photoconversion, respectively. Light was applied until photoequilibrium was achieved, and efficient photoconversion (>90%) was confirmed using acid denaturation, with NpR6012g4 and RcaE as references.[8,14,32] The resulting spectra were normalized for comparison to those of NpR6012g4 (Figure 1B). The optical densities of the samples were adjusted to 1.5−3.0 (per centimeter) at the peak wavelengths for transient measurements.

Transient Signals. The ultrafast primary (125 fs−7 ns) dynamics of both forward ($^{15Z}P_r \rightarrow {}^{15E}P_g$) and reverse ($^{15E}P_g \rightarrow {}^{15Z}P_r$) photoreactions of AnPixJg2 were measured as previously discussed.[44] The excitation pulses originate from a Ti:sapphire-amplified laser (SpectraPhysics SpitFire Pro) that pumps two homemade single-pass noncollinear optical parametric amplifiers (NOPAs). The excitation wavelengths used for initiating the forward (640 nm) and reverse (520 nm) primary signals were selected to be near the peaks of the static absorption spectra of AnPixJg2 (Figure 1B). The polarization of the pump beam was set at the magic angle (54.7°) with respect to the probe beam to avoid anisotropic effects. Broadband probe pulses were generated by focusing a portion (~1 μJ) of the 800 nm laser beam into a slowly translating 2 mm thick CaF$_2$ crystal. After passing the sample, the probe pulses were imaged via a spectrograph (Oriel Instruments 77480) onto a 512-pixel silicon diode array (Hamamatsu C7884-8L003). A linear polarizer set to 90° to pump light polarization was added before the spectrograph to aid in reducing pump scatter from the signals. The temporal resolution of the ultrafast experiments was estimated to be 125 fs on the basis of the rise times of the signals of a dye molecule.

Secondary forward and reverse dynamics for AnPixJg2 have previously been reported by Fukushima et al.[26] Secondary forward dynamics for NpR6012g4 were already reported by Lim et al.,[29,30] and secondary (7 ns−10 ms) reverse reaction dynamics for NpR6012g4 were obtained in a manner similar to that of the primary reaction measurements, except that the 532 nm excitation pulses were generated from an independently operating Q-switched diode-pumped solid-state YAG laser (Pulselas-A-532-300). The full setup is described elsewhere.[45] Probe delays were controlled by delaying the YAG excitation pulses electronically. The time resolution was estimated to be ~550 ps on the basis of the rise times of the signals.

To ensure a fresh sample for each excitation, the solutions were flowed in a closed tubing circuit with a 2 mm path-length quartz cuvette. To maintain CBCRs in their $^{15Z}P_r$ state during the forward reaction experiments, samples were continuously illuminated prior to entering the cuvette with ~5 mW of a green (532 nm) actinic laser diode. For the reverse dynamics measurements, a 630 nm laser diode (5 mW) was used to maintain samples in their $^{15E}P_g$ state.

FTIR Signals. A commercial FTIR instrument (Tensor 27, Bruker Optics) was modified with a lab platform (Thorlabs, 23.8 cm × 25.5 cm) to hold two laser diodes and a motorized flipper (Thorlabs mff 101). Samples were illuminated with the same 630 and 532 nm laser diodes used in transient experiments

described above to shift the sample between the $^{15Z}P_r$ and $^{15E}P_g$ states, respectively. A motorized flipper was used to overcome detector drift, which was placed inside the sample compartment of the FTIR instrument (Figures S2 and S3). To purge the sample chamber of moisture, a liquid nitrogen (LN2) system consisting of a liquid nitrogen tank, a copper coil, a desiccant column, and a flowmeter was built (Figure S4).

Samples were placed between two CaF$_2$ windows, and the FTIR instrument was sealed and purged overnight (~12 h) with nitrogen in a dark environment. The instrument was purged overnight with a flow rate of 1 L min^{-1}, which was increased to 4 L min^{-1} during data collection. Samples were illuminated for 10 min with 532 nm light to probe the $^{15Z}P_r$ state followed by 20 background and sample scans (flipper moving up and down). This was repeated with 630 nm light to probe the $^{15E}P_g$ state. The average light−dark ($^{15E}P_g$−$^{15Z}P_r$) difference spectrum was calculated according to the following equation:

$$\Delta A(\nu) = A_{light}(\nu) - A_{dark}(\nu) \qquad (1)$$

Global Analysis. Ultrafast TA signals typically consist of four overlapping signals: (1) negative ground-state bleach (GSB) from the loss of ground-state absorption (GSA), (2) negative stimulated emission (SE) from the photostimulated decay of the excited state, (3) positive excited-state absorption (ESA) from $S_1 \rightarrow S_n$ transitions, and (4) positive photo-intermediate absorptions attributed to photogenerated ground-state populations. Transient data sets were analyzed with a multicompartment global analysis formalism[46,47] that decomposes the transient data via a postulated model into time-dependent concentrations with time-independent spectra. This is accomplished by fitting the data with the numerical solutions of linear first-order differential equations describing the postulated target model (eq 2)

$$\frac{dn_i}{dt} = A_i I(t) + \sum_{i,j} K_{i,j} n_i(t) \qquad (2)$$

where n_i represents the ith microscopic population of interest, A_i is the occupancy of the ith excited state, $I(t)$ is the pump pulse temporal envelope, and K_{ij} values are the rate constants describing the exponential evolution of the ith population into the jth population. If the underlying target model accurately describes the dynamics, the extracted spectra from the analysis are termed species-associated difference spectra (SADS) and represent the true difference spectra of the constituent populations. However, if the model inaccurately describes the dynamics, the resulting spectra from the global analysis are combinations of the true SADS.[21,23,46,47]

A sequential model (A → B → C ...) is a commonly used model in the analysis of broadband TA data that posits multiple populations sequentially evolve one into the other via unidirectional steps. The spectra extracted from this model are called "evolution-associated difference spectra" (EADS). If the underlying photodynamics of the system are truly sequential, then the EADS are also SADS. However, if the system exhibits nonsequential (e.g., branched or parallel) or reversible dynamics, then the EADS are mixtures of SADS and extracting the SADS requires construction of more complex models.[21,22,46,47] Fitting the TA signals with a sequential model provides important *a priori* constraints on population flow, which is useful for constructing feasible target models to obtain SADS. This approach was used to construct an inhomogeneous
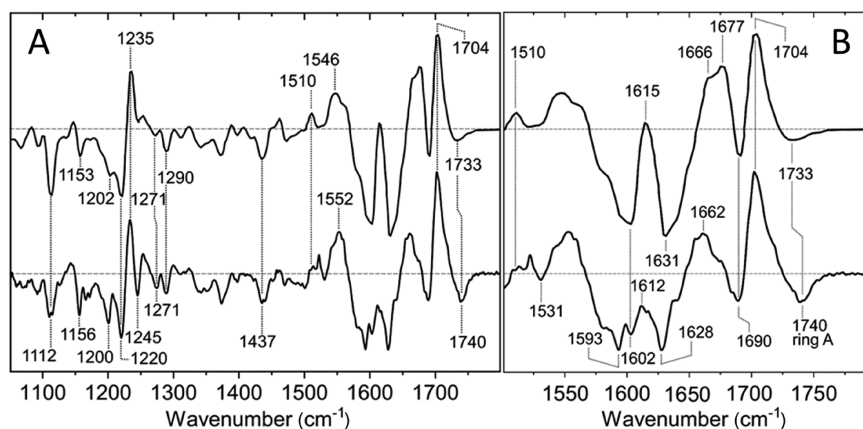
Figure 2. (A) P_g-P_r difference IR absorption spectra of AnPixJg2 (top) and NpR6012g4 (bottom). Negative signals correspond to the $^{15Z}P_r$ state, whereas positive peaks correspond to structural changes toward $^{15E}P_g$-state formation. (B) Detailed view of the FTIR difference spectrum in the spectral range of 1800−1500 cm^{-1}. Band assignments are based on previous work.[49]
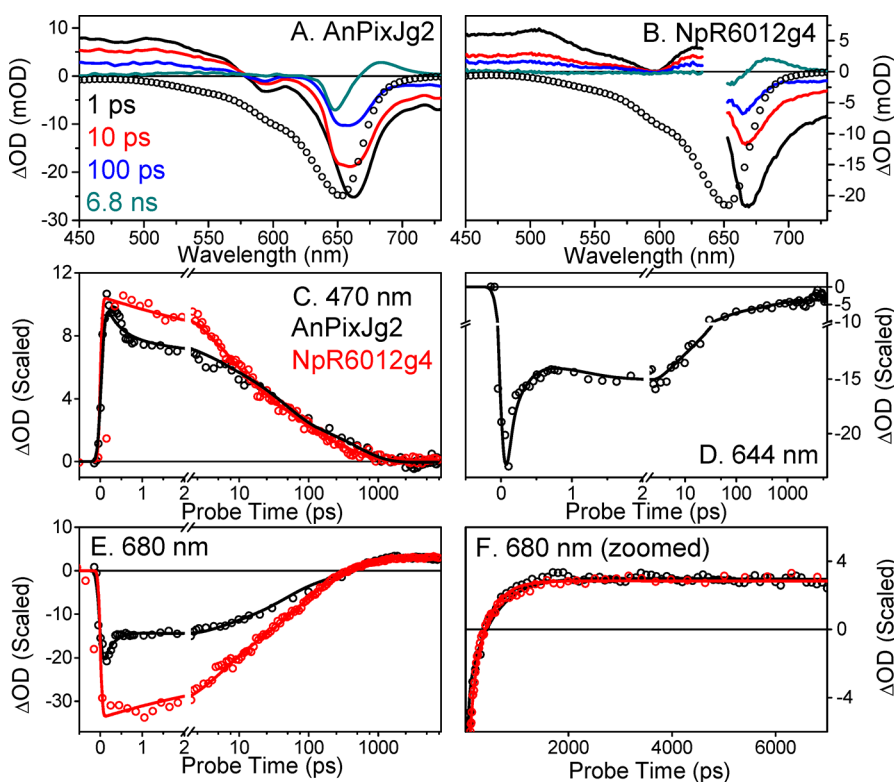

Figure 3. Comparison of the transient absorption spectra for ultrafast forward ($^{15Z}P_r \rightarrow ^{15E}P_g$) dynamics in (A) AnPixJg2 and (B) NpR6012g4.[21] Ground-state absorption spectra of $^{15Z}P_r$ states are shown as empty circles. Probe times in both panels are indicated in panel A. (C−F) Comparison of the selected scaled kinetics for ultrafast forward ($^{15Z}P_r \rightarrow ^{15E}P_g$) dynamics in AnPixJg2 and NpR6012g4.[21] NpR6012g4 was not included in the 644 nm kinetic trace (D) because this wavelength was excised due to pump scatter. Empty circles represent data, and solid curves are the fits to the global model outlined in Figure 6. NpR6012g4 (red curves) kinetics were scaled with a factor of 1.73 to match the amplitude of the AnPixJg2 signal at 475 nm at 0.1 ps (explained below). NpR6012g4 data around 650 nm are excised for presentation due to pump scatter. AnPixJg2 data around 650 nm contain minimal pump scatter because the polarizer was used to block it.

model to analyze the secondary forward dynamics of NpR6012g4.[21,30]

■ RESULTS

The static electronic absorption spectra of $^{15Z}P_r$ and $^{15E}P_g$ in both AnPixJg2 and NpR6012g4 are remarkably similar (Figure 1B). Both CBCRs, like most other representatives of the red/green family,[20,21,23,25,33] exhibit dark-adapted red-absorbing $^{15Z}P_r$ spectra (with a high-energy shoulder at 600 nm) and

light-adapted green-absorbing $^{15E}P_g$ states. The $^{15Z}P_r$ and $^{15E}P_g$ spectra of AnPixJg2 are slightly blue-shifted and red-shifted compared to those of NpR6012g4, respectively. Both sets of spectra have similar relative amplitudes, indicating comparable ratios of the extinction coefficients for the states in the respective CBCRs.

Both AnPixJg2 and NpR6012g4 also exhibit similar difference FTIR $^{15E}P_g-^{15Z}P_r$ difference spectra (Figure 2). We observe chromophore peaks in the same intensity range as amide peaks,

indicating a rather localized structural change (see ref 38 for more details) and the absence of major protein structural rearrangements observed in distantly related systems such as prototypical and bathy phytochromes.[48,49] In agreement with previous work, we observe the characteristic difference peaks assigned to the chromophore C=O stretching modes of rings A and D in the $^{15Z}P_r$ (−) and $^{15E}P_g$ (+) states in AnPixJg2.[37,38] These correspond to the peak pair at 1690(−)/1704(+) cm^{-1} assigned to the carbonyl group of the D-ring and the negative signal at 1733 cm^{-1} assigned to the C=O group of the A-ring in the $^{15Z}P_r$ state (Figure 2, top spectra). The corresponding positive peak from the A-ring of the $^{15E}P_g$ state is obscured by the dominant D-ring signal. In NpR6012g4, we observe an identical signature of the D-ring C=O difference band, whereas the C=O peak of the $^{15Z}P_r$ state is upshifted to 1740 cm^{-1} (Figure 2, bottom spectra). In addition, the amide region displays some discrepancies that might originate from a lower difference signal intensity in NpR6012g4 that reflects either a lower concentration or a lower level of $^{15Z}P_r$ to $^{15E}P_g$ photoconversion.

While the overall structural and spectroscopic similarity of the $^{15Z}P_r$ states is striking, the discrepancies in the A-ring C=O peak ($^{15Z}P_r$ state) suggest slightly different chromophore−protein interactions in NpR6012g4 and AnPixJg2.

Forward ($^{15Z}P_r \rightarrow {}^{15E}P_g$) Reaction Photodynamics. The transient spectra of the forward reaction dynamics of both AnPixJg2 and NpR6012g4 are compared in panels A and B of Figure 3 at selected probe times.[21] The dynamics of both CBCRs exhibit similar initial spectra attributed to the excited-state $^{15Z}P_r$* population(s) with a broad positive ESA band from 450 to 570 nm and a pronounced negative GSB/SE band peaking around 670 nm. The 570−630 nm region has been shown to be CBCR-dependent[20] and is negative in AnPixJg2 (Figure 3A) and positive in NpR6012g4 (Figure 3B). After the $^{15Z}P_r$* population(s) has decayed, a difference spectrum is observed with a positive band at 675 nm and a negative GSB at 650 nm (teal curves). This is ascribed to the gain of the primary Lumi-R$_f$ photointermediate and the concomitant loss of $^{15Z}P_r$.

The 470 nm kinetics of both CBCRs (Figure 3C) track the decay of the excited-state $^{15Z}P_r$* population(s), and the 680 nm kinetics (Figure 3E) track the decay of the ground-state bleach (GSB) signals and the growth of the Lumi-R$_f$ photointermediate. The AnPixJg2 signals (Figure 3C−E, black curve) exhibit a fast 300 fs phase that is noticeably absent in the NpR6012g4 signals (red curves). Three potential origins are considered for this phase. (1) It may be a "coherent artifact" (i.e., a mixture of cross-phase modulation, two-photon absorption, and stimulated Raman scattering).[50] (2) It may result from the rapid relaxation of a Franck−Condon region of the $^{15Z}P_r$* population into a more relaxed population. (3) It may be ascribed to a $^{15Z}P_r$* subpopulation with a very short lifetime. On the basis of the justifications given below, this fast relaxation phase is ascribed to a rapidly evolving subpopulation.

The kinetics of AnPixJg2 and NpR6012g4 were scaled to match the ESA at 475 nm at 0.1 ps. The resulting scaled kinetics at 680 nm exhibit a filling of the GSBs and a plateauing of the Lumi-R$_f$ signal (Figure 3E,F). Because the amplitude of the GSB at 680 nm for AnPixJg2 is smaller than that for NpR6012g4, while giving the same Lumi-R$_f$ signal, this may suggest a higher quantum yield for AnPixJg2. However, in view of the different overlap of the GSB and Lumi-R$_f$ bands for AnPixJg2 and NpR6012g4, a different interpretation may be more prudent. To estimate the quantum yield of generating Lumi-R$_f$ (Φ_p) for the two CBCRs, their 0.1 ps and 1 ns spectra were compared (Figure

4). The scaled 0.1 ps spectra exhibited similar amplitudes of GSB signals (Figure 4A, solid curves). When scaled to the same factor
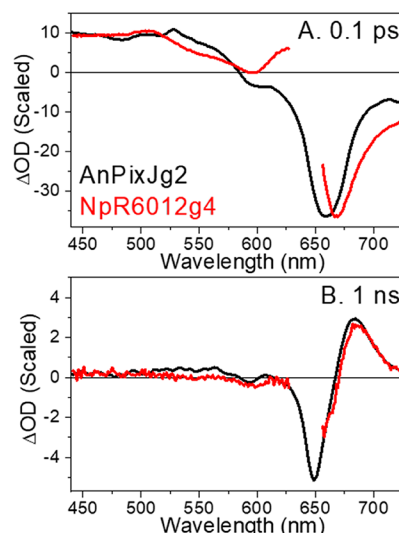

Figure 4. Comparison of (A) 0.1 ps and (B) 1 ns spectra of the forward ($^{15Z}P_r \rightarrow {}^{15E}P_g$) dynamics in AnPixJg2 (black curves) and NpR6012g4 (red curves) scaled at 475 nm to the amplitude of the AnPixJg2 signal at 0.1 ps.[21] The same scaling factor was used for the 1 ns spectra.

that was used for the comparison in Figure 4A, the 1 ns spectra displayed identical Lumi-R$_f$ signal amplitudes at 680 nm (Figure 4B). The similar amplitudes of both photointermediate spectra at 1 ns indicate that the Φ_p values are nearly identical at ~40% for both AnPixJg2 and NpR6012g4.[23]

We next leveraged multiwavelength global analysis to interpret the TA signal kinetics with a four-population heterogeneous model for AnPixJg2 (Figure 5 and Table 1) that is similar to the three-population heterogeneous model adopted by Kim et al. for NpR6012g4 (Figure 5A[23] and Figure S6[21]). The applicability of such a model was supported by an EADS analysis, using normalized and differences of normalized EADS (Figure S5). The model used for NpR6012g4 (Figure 5B) is described in detail elsewhere.[23] The primary difference between the optimized models used here for AnPixJg2 was the inclusion of a short-lived excited-state population (ESI0) with a 300 fs lifetime that was not observed in the NpR6012g4 measurements (Figure 3C−E, black curves). The more slowly relaxing excited-state populations (ESI1−ESI3) were observed in both CBCRs with comparable lifetimes, although the lifetime of ESI3 for AnPixJg2 of 490 ps was significantly longer than NpR6012g4's ESI3 lifetime of 310 ps.

While the "nonphotoisomerized" GSI intermediate in NpR6012g4 is long-lived ($\tau_{apparent}$ = 10 ps),[23] a comparable, albeit broader absorbing (Figure 5C), population observed in AnPixJg2 is appreciably shorter-lived ($\tau_{apparent}$ = 0.6 ps) and produced in a lower abundance. In AnPixJg2, the 470 and 644 nm kinetics (Figure 3C,D and Figure S7) resolves a quickly evolving excited-state subpopulation that populates a red-shifted population on an ~300 fs time scale. This red-shifted population then decayed within 2 ps (Figure 3D and Figure S7) and was ascribed to a GSI. This excited-state subpopulation is too short-lived to be characterized by pump-dump-probe spectroscopy[23] but is believed to be unproductive because there was not a rise in the Lumi-R$_f$ kinetic trace on this time scale (Figure 3E).
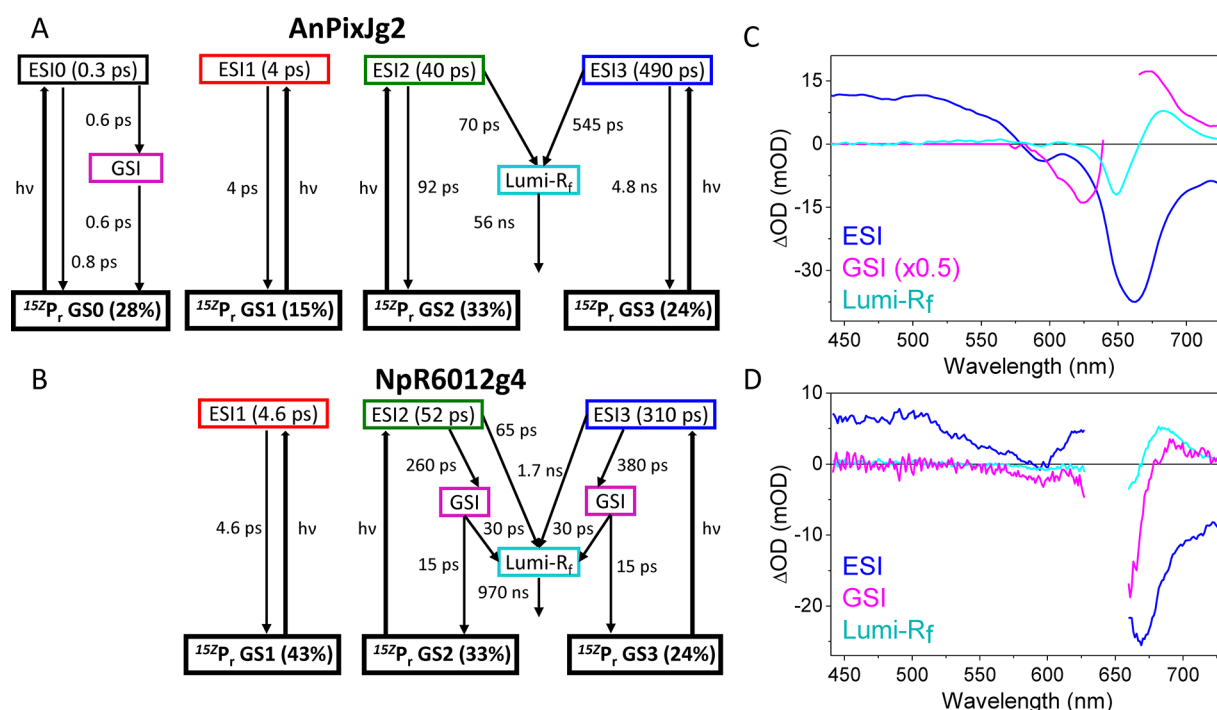
Figure 5. Comparison of AnPixJg2 (first row, A and C) and NpR6012g4[23] (second row, B and D) global analysis models (first column, A and B) and species-associated difference spectra (SADS, second column, C and D). Unique ESI spectra and concentration profiles are shown in Figure S6. The GSI of AnPixJg2 was forced to be zero up to 570 nm.

Table 1. Parameters for Target Analysis of the Primary Forward Reaction ($^{15Z}P_r \to {}^{15E}P_g$) Dynamics of AnPixJg2 and NpR6012g4 (Figure 5A and 5B)[23,a]

	AnPixJg2						
	ESI0		ESI1		ESI2		ESI3
occupancy (%)	28		15		33		24
$\tau_{apparent}$ (ps)	0.3		4		40		490
	$\to$ GSI	$\to {}^{15Z}P_r$ GS0	$\to {}^{15Z}P_r$ GS1	$\to$ Lumi-R_f	$\to {}^{15Z}P_r$ GS2	$\to$ Lumi-R_f	$\to {}^{15Z}P_r$ GS3
τ	0.6 ps	0.8 ps	4 ps	70 ps	92 ps	545 ps	4.8 ns
branching yield (%)	57	43	100	57	43	89	11
Φ_b (%)	–	–	–	18.8	–	21	–
total Φ_p (%) (Lumi-R_f)				39.8			

	NpR6012g4				
	ESI1		ESI2		ESI3
occupancy (%)	43		33		24
$\tau_{apparent}$ (ps)	4.6		52		310
	$\to {}^{15Z}P_r$ GS1	$\to$ Lumi-R_f	$\to {}^{15Z}P_r$ GS2	$\to$ Lumi-R_f	$\to {}^{15Z}P_r$ GS3
τ	4.6 ps	65 ps	260 ps	1.7 ns	380 ps
branching yield (%)	100	80	20	18.2	81.8
Φ_b (%)	–	26.4	–	4.4	–
Φ_{GSI} (%)	–	–	2.2	–	6.4
total Φ_p (%) (Lumi-R_f)			39.4		

[a]A three-population model was also used to model the primary forward reaction of AnPixJg2 (Table S1 and Figure S6).

AnPixJg2 exhibits an excited-state lifetime that is ~10% shorter than that of NpR6012g4 and does not have discernible GSI production from longer-lived ESI2 and ESI3. For both CBCRs, Lumi-R_f is not generated from the shorter-lived populations but appears only later, i.e., in the transition from EADS3 to EADS4, as suggested by the differences in normalized EADS (Figure S5C). For this reason, only ESI2 and ESI3 are modeled to generate Lumi-R_f. The fitting of the Lumi-R_f decay region (Figure 5A) estimates a lifetime of 56 ns for Lumi-R_f in

AnPixJg2, while that for NpR6012g4 extracted from Lim et al. is 970 ns (Figure 5B).[30]

Secondary Forward Dynamics. The evolution of Lumi-R_f into subsequent intermediates to generate $^{15E}P_g$ has been reported for both AnPixJg2[26] and NpR6012g4.[29,30] The secondary TA kinetics and spectra for NpR6012g4 are reproduced[29,30] in panels A and B of Figure 6 and are remarkably similar to the previously reported AnPixJg2 signals.[26] For both CBCRs, a monotonically blue-shifting series
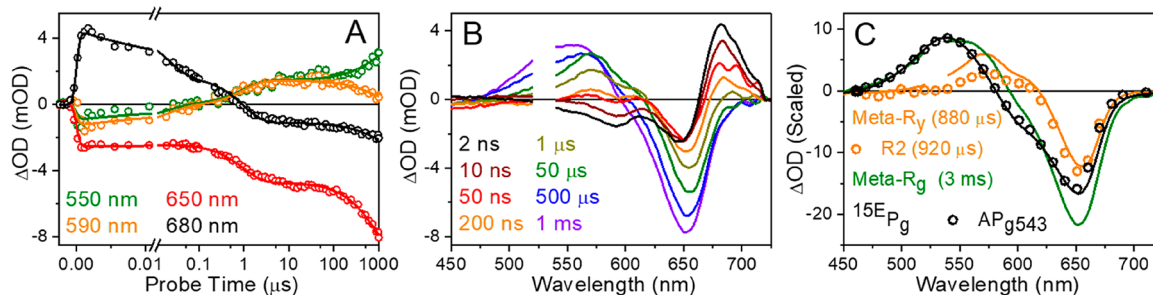
Figure 6. Transient absorption signals for the secondary forward ($^{15Z}P_r \rightarrow {}^{15E}P_g$) dynamics of NpR6012g4.[30] (A) Kinetic traces at wavelengths specified in the legend. Wavelengths were chosen to represent important spectral features [photoproduct(s), bleach, etc.]. Data (empty circles) are overlaid with fits (solid curves) from the sequential model. (B) Difference spectra at select probe times. (C) Comparison of the extracted EADS of the secondary forward ($^{15Z}P_r \rightarrow {}^{15E}P_g$) dynamics in AnPixJg2[26] [R2 and AP$_{g543}$ (empty circles)] and NpR6012g4 [Meta-R$_y$, Meta-R$_g$, and $^{15E}P_g$ (solid curves)].[30] The respective decay constants are given in parentheses.
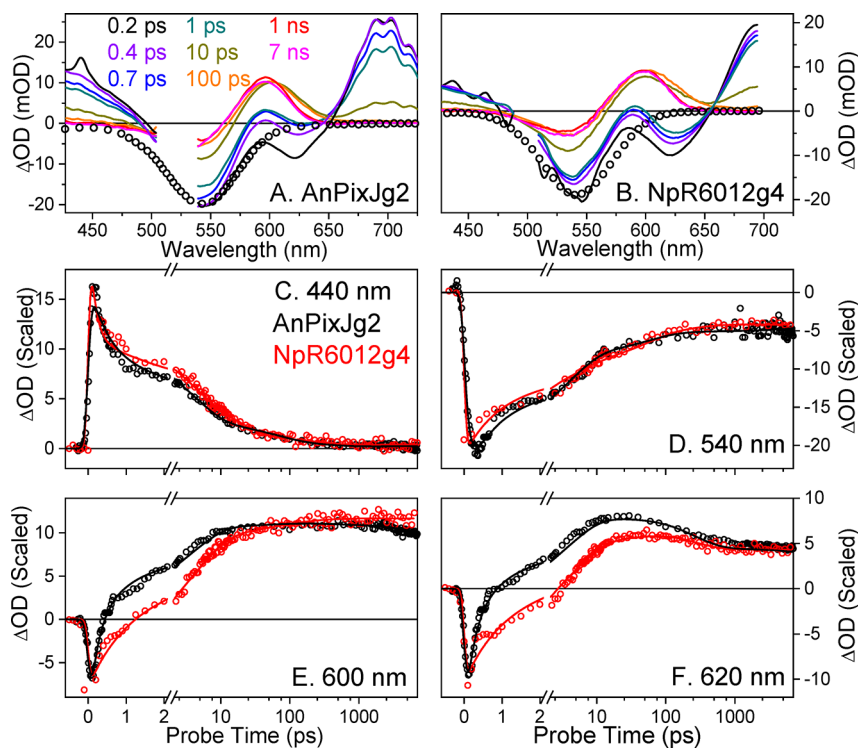

Figure 7. Comparison of the transient absorption spectra for ultrafast reverse ($^{15E}P_g \rightarrow {}^{15Z}P_r$) dynamics in (A) AnPixJg2 excited with a 520 nm light pulse and (B) NpR6012g4 excited with 500 nm light pulse.[22] Ground-state absorption (GSA) of $^{15E}P_g$ is shown with empty circles. The set of time points in the legend of panel A is the same for both panels. (C–F) Comparison of the scaled at 150 fs selected kinetics for primary reverse ($^{15E}P_g \rightarrow {}^{15Z}P_r$) dynamics in AnPixJg2 (black curves) and NpR6012g4[22] (red curves). Empty circles represent raw data, and solid lines represent global analysis fit curves from the model in Figure 9.

of intermediates following the red-shifted Lumi-R$_f$ preceded formation of the $^{15E}P_g$ photoproduct.

EADS obtained for the secondary forward reaction of AnPixJg2 by Fukushima et al.[26] are compared to those of NpR6012g4[30] in Figure 6C. Meta-R$_y$ in NpR6012g4 (Figure 6C, orange curve) and R2 in AnPixJg2 (Figure 6C, orange empty circles) absorb in the same spectral region and have comparable lifetimes of 880 and 920 μs, respectively. For AnPixJg2, Meta-R$_y$ (R2) represents the only detected intermediate in the secondary forward reaction prior to formation of the $^{15E}P_g$ (AP$_{g543}$) photoproduct in 5 ms.[26] For NpR6012g4, Meta-R$_y$ evolves to Meta-R$_g$ (τ = 3 ms) prior to yielding $^{15E}P_g$. Thus, the secondary forward reaction in NpR6012g4 has an additional step not observed for AnPixJg2.

Reverse ($^{15E}P_g \rightarrow {}^{15Z}P_r$) Reaction Photodynamics. The selected ultrafast transient spectra of the reverse reaction of AnPixJg2 and NpR6012g4[22] exhibit similar positive and negative band evolution (Figure 7A,B). Both domains have negative GSB bands at 540 nm and SE bands at 625 nm with positive flanking ESA bands, The excited-state population partially evolves to a Lumi-G$_o$ photointermediate band at 610 nm that later blue-shifts to the Meta-G$_o$ intermediate at 600 nm. Nevertheless, there are key differences in the shapes of the transient spectra. The SE band in NpR6012g4 has a negative value peaking at 620 nm, whereas the SE band in AnPixJg2 is shifted and contributes to the depression of the ESA band at 635 nm, resulting in the signal close to zero. The SE band in AnPixJg2 clearly decays faster than the SE in NpR6012g4 (Figure 7E and 7F, black and red curves).

As the 440 nm kinetics (Figure 7C) demonstrate, the excited $^{15E}P_g^*$ state of AnPixJg2 decays slightly faster than that of NpR6012g4 with faster formation of the Lumi-G_o photo-intermediate (Figure 7F). However, at later times (50 ps−7 ns), the 620 nm kinetics decay on comparable time scales for both photoreceptors, pointing to the same time for blue-shifting kinetics from Lumi-G_o to Meta-G_o. The 600 nm kinetics of AnPixJg2, in contrast to that of NpR6012g4, shows clear decay of Meta-G_o in the studied time range.

The reverse reaction Φ_p for generating the primary Lumi-G_o intermediate was estimated by scaling of the selected raw spectra in the same manner that was used for the forward reaction described above (Figure 8A). Scaling with the same scaling
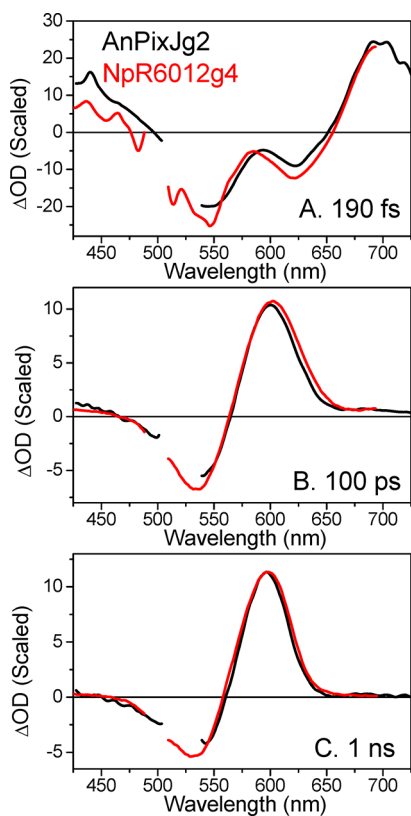

Figure 8. Comparison of (A) 190 fs, (B) 100 ps, and (C) 1 ns transient spectra of reverse $(^{15E}P_g \rightarrow {}^{15Z}P_r)$ dynamics in AnPixJg (excited at 520 nm) and NpR6012g4 (excited at 500 nm)[21] scaled at 600 nm to the amplitude of the AnPixJg2 signal at 1 ns. The same scaling factor (1.17) was used for 190 fs and 100 ps spectra. Scatter regions for AnPixJg2 around 520 nm and for NpR6012g4 around 500 nm are excised. A comparison to the spectra at 190 fs and 1 ns of NpR6012g4 excited at 575 nm is shown in Figure S8.

factor of 1 ns (Figure 8C) and 190 fs (Figure 8A) spectra of the reverse $(^{15E}P_g \rightarrow {}^{15Z}P_r)$ reaction of AnPixJg2 and NpR6012g4 estimates nearly identical Φ_p values. Φ_p is dependent on the excitation wavelength as shown for NpR6012g4 excited at 575 nm; its reaction yield was estimated to be 48% compared to 56% upon excitation at 500 nm.[22] While the excitation of AnPixJg2 with higher-energy light may result in a higher yield, this comparison was not performed.

The three-population model constructed for the primary reverse dynamics of NpR6012g4[22] (Figure 9) also satisfactorily fits the AnPixJg2 reverse signals (Figure 7C−F, solid curves). This model resembles the model adopted for the forward

reaction with three coexisting ground-state $^{15E}P_g$ populations that when photoexcited generate three $^{15E}P_g^*$ excited-state intermediates (ESIs). However, in contrast to the forward dynamics model, only the two fastest ESIs exhibit measurable quantum yields in generating the primary Lumi-G_o intermediate (peaking at 610 nm), which rapidly (∼250 ps) evolves into the blue-shifted Meta-G_o intermediate (peaking at 600 nm). According to the analysis of the secondary reverse dynamics of NpR6012g4 (*vide infra*), the lifetime for its Meta-G_o (or Meta-G_{o1} as renamed in the secondary dynamics analysis) is shorter (18 ns), and we would expect to see an even clearer decay of Meta-G_o (or Meta-G_{o1}) of NpR6012g4 in the 600 nm kinetics. However, the decay of the kinetics is not observed possibly because Meta-G_o (or Meta-G_{o1}) is followed by spectrally similar Meta-G_{o2}, which decays with a time constant of 140 ns. The appearance of the latter photointermediate (Meta-G_{o2}) may compensate for the decay of Meta-G_o (or Meta-G_{o1}) and make the 600 nm kinetic nondecaying observed by Kim et al.[22] in Figure 9E (red curve).

The population occupancies differ, suggesting shorter-lived ESI species are more abundant in AnPixJg2, which agrees with the faster excited-state decay kinetics (Figure 7C−F, black curves). The branching ratio for the photointermediate yield (Table 2) indicates Lumi-G_o in AnPixJg2 is populated in comparable proportions from ESI1 and ESI2. In contrast, ESI1 contributes one-third and ES2 contributes two-thirds to the total Lumi-G_o yield in NpR6012g4. This also explains the earlier appearance of Lumi-G_o in AnPixJg2 data (Figure 7E,F). As mentioned above, the extrapolation during fitting gives a 75 ns lifetime constant for Meta-G_o in AnPixJg2, which is supported by the observed decay of the 600 nm kinetic trace (Figure 7E, black curve). The SADS for Lumi-G_o and Meta-G_o are identical in AnPixJg2 and NpR6012g4 (Figure S10).

The secondary dynamics of both CBCRs exhibit non-monotonic and multiphasic evolution. The TA spectra and kinetics of NpR6012g4 are shown in panels A and B of Figure 10. The evolution starts with a 610 nm band that blue-shifts to 585 nm at hundreds of nanoseconds. The latter then red-shifts to 640 nm at 1 ms.

The secondary reverse dynamics of NpR6012g4 were fit to a six-compartment sequential model (Figures 10C and 11): Lumi-G_o (263 ps), Meta-G_{o1} (18 ns), Meta-G_{o2} (140 ns), Meta-G_{y1} (870 ns), Meta-G_{y2} (1.6 ms), and Meta-G_r (infinity). The reaction starts with Lumi-G_o [at 610 nm (Figure S11)], which further blue-shifts to Meta-G_{o1} and Meta-G_{o2} [at 600 nm (Figure S11)]. Another blue-shift to Meta-G_{y1} and Meta-G_{y2} (at 585 nm) follows. The necessity of splitting into these spectrally identical components (Meta-G_{o1} and Meta-G_{o2} at 600 nm; Meta-G_{y1} and Meta-G_{y2} at 585 nm) is dictated by the phases observed in the data. Elimination of the splitting gives inadequate fitting. The final stage observed in the studied time window is the red-shift to Meta-G_r (at 640 nm). Both orange-absorbing EADS [Meta-G_{o1} and Meta-G_{o2} (Figure 10C, red and blue curves)] are spectrally identical as are the two yellow-absorbing EADS [Meta-G_{y1} and Meta-G_{y2} (Figure 10C, green and cyan curves)] (Figure S12). Removing the orange Meta-G_{o2} or the yellow Meta-G_{y2} compartment from the model gives an appreciably poorer fit that cannot describe the nonmonotonic kinetics at 575 nm (Figure 10B, green curve).

The nonmonotonic kinetics is a consequence of a spectral band amplitude decrease of ∼30% with the transition from Meta-G_{o1} to Meta-G_{o2} (Figure 10C, red and blue curves) and another 30% with the transition from Meta-G_{y1} to Meta-G_{y2}
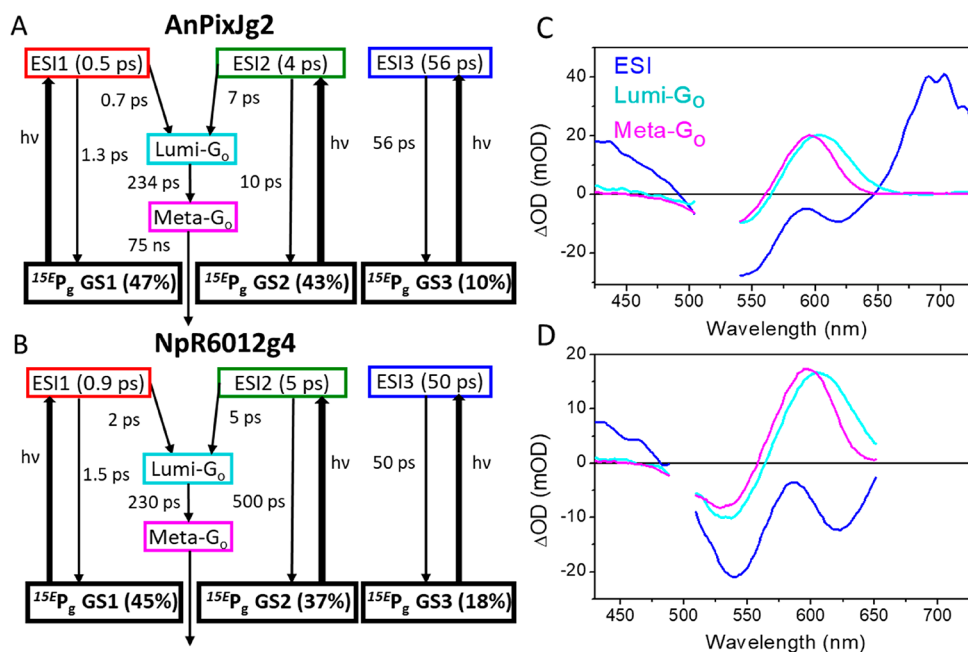
Figure 9. Comparison of AnPixJg2 (excited at 520 nm, first row, A and C) and NpR6012g4[22] (excited at 500 nm, second row, B and D) ultrafast global analysis models (first column, A and B) and species-associated difference spectra (SADS, second column, C and D). Scatter regions for the AnPixJg2 spectrum around 520 nm and for the NpR6012g4 spectrum around 500 nm are excised. Blue curve represents all three ESIs (ESI1−ESI3). Concentration profiles are shown in Figure S9.

Table 2. Parameters for Target Analysis of the Primary Reverse Reaction ($^{15E}P_g \rightarrow ^{15Z}P_r$) Dynamics of AnPixJg2 and NpR6012g4 (Figure 9A and 9B)[22]

	AnPixJg2					
	ESI1			ESI2		ESI3
occupancy (%)	47			43		10
$\tau_{apparent}$ (ps)	0.5			4		56
	$\rightarrow$ Lumi-G$_o$	$\rightarrow ^{15E}P_g$ GS1		$\rightarrow$ Lumi-G$_o$	$\rightarrow ^{15E}P_g$ GS2	$\rightarrow ^{15E}P_g$ GS3
τ (ps)	0.7	1.3		7	10	56
branching yield (%)	65	35		59	41	100
Φ_b (%)	30.5	–		25	–	–
total Φ_p (%) (Lumi-G$_o$)			55.5			
	NpR6012g4					
	ESI1			ESI2		ESI3
occupancy (%)	45			37		18
$\tau_{apparent}$ (ps)	0.9			5		50
	$\rightarrow$ Lumi-G$_o$	$\rightarrow ^{15E}P_g$ GS1		$\rightarrow$ Lumi-G$_o$	$\rightarrow ^{15E}P_g$ GS2	$\rightarrow ^{15E}P_g$ GS3
τ (ps)	2	1.5		5	500	50
branching yield (%)	43	57		99	1	100
Φ_b (%)	19	–		36.6	–	–
total Φ_p (%) (Lumi-G$_o$)			55.6			

(Figure 10C, green and cyan curves). Although the sequential evolution between the two orange photointermediates (from Meta-G$_{o1}$ to Meta-G$_{o2}$) and between the two yellow photointermediates (from Meta-G$_{y1}$ to Meta-G$_{y2}$) is descriptive of the dynamics, it may not correspond to the true transition from one transient intermediate to another because the absorption remains spectrally comparable (Figure S12). A more likely model is that the loss of the amplitude corresponds to the decay of the first intermediate of each spectral pair back to the P$_g$ state. To model this shunt population, a more complex analysis is necessary; however, the simpler sequential modeling is capable of resolving both the shunting time scale and branching yields by simple inspection of the EADS amplitudes (Figures 10C and

11). After the first shunt, 0.7 of the initially isomerized population (Lumi-G$_o$) propagates into the photoreaction (Figure 10C, red and blue curves). After the second shunt, only 0.7 × 0.7 = 0.49 of the population proceeds to the completion of the reaction (Figure 10C, green and cyan curves). This suggests approximately half of the Lumi-G$_o$ photointermediate yield [Φ_p = 55.5% (Table 2)] in NpR6012g4 contributes to the total reaction yield (Φ) that is estimated to be 27%.

The AnPixJg2 secondary reverse ($^{15E}P_g \rightarrow ^{15Z}P_r$) dynamics characterized by Fukushima et al.[26] was compared with the final phases of the NpR6012g4 reverse dynamics (Figure 12). The G1 photointermediate in AnPixJg2 spectrally resembles Meta-

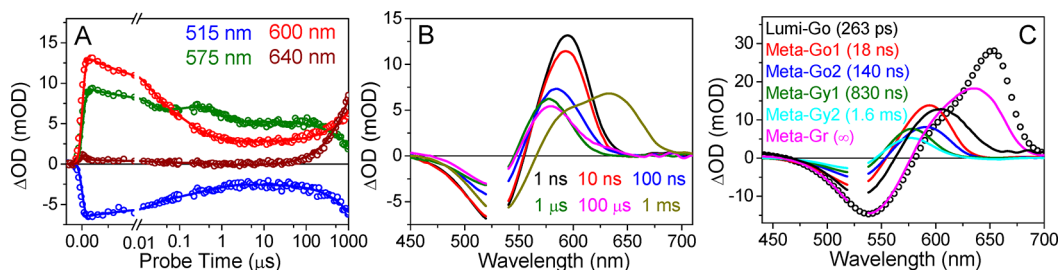**Figure 10.** Transient absorption signals for secondary reverse ($^{15E}P_g \rightarrow {}^{15Z}P_r$) dynamics of NpR6012g4. (A) Kinetic traces at wavelengths specified in the legend (empty circles). Wavelengths were chosen to represent important spectral features [photointermediate(s), bleach, etc.]. Data are overlaid with fits (solid curves) from a sequential model with EADS shown in panel C. (B) Spectra at selected probe times. (C) EADS with kinetic parameters shown in parentheses. The $^{15Z}P_r$–$^{15E}P_g$ difference spectra (empty circles) are added for comparison.
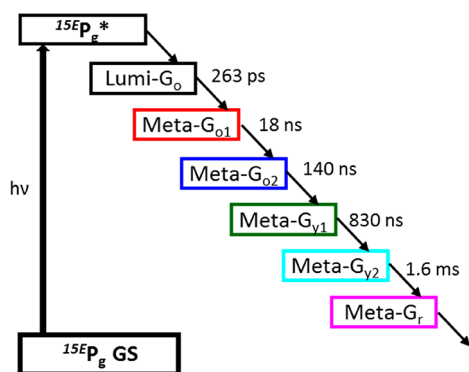

Figure 11. Sequential model of the secondary reverse dynamics of NpR6012g4.

G_{y1} and Meta-G_{y2} in NpR6012g4 (Figure 12A, orange empty circles and orange solid curve). However, the AnPixJg2 G1 spectrum contains a second spectral band near 680 nm (Figure 12B), pointing to the existence of the far-red Meta-G_f photointermediate at 680 nm (Figure 12B, orange empty circles).

■ DISCUSSION

Comparison of the primary and secondary dynamics of the forward and reverse reaction mechanisms of AnPixJg2 and NpR6012g4 resolved striking similarities (Scheme 2). The forward reaction of both NpR6012g4 and AnPixJg2 resolved an initial intermediate that was red-shifted from the GSB and evolved through a series of blue-shifted intermediates prior to

populating the $^{15E}P_g$ signaling state (Figures 5 and 6). These spectral trends were observed to be nearly conserved across eight red/green CBCRs isolated from *N. punctiforme*.[29] The reverse reaction of both CBCRs consisted of nonmonotonic spectral evolution in which the first intermediate was red-shifted from the GSB that initially blue-shifted prior to red-shifting through at least one intermediate before populating the $^{15Z}P_r$ photoproduct (Figures 9, 10, and 12). Despite the overall similarities, we observed key differences in the photochemical dynamics of the two proteins. Notable differences in the forward reaction include the much slower evolution of the primary Lumi-R_f photointermediate (Figure 5), the presence of a kinetically resolved long-lived Meta-R_g intermediate (Figure 6), and the previously identified GSI[23] in NpR6012g4. Notable differences in the reverse reaction include partial photointermediate shunts unique to the reverse reaction of NpR6012g4 (Figure 10) and a Meta-G_f population red-shifted from $^{15Z}P_r$ unique to AnPixJg2 (Figure 12B). Finally, we note that the thermal recovery times of the two CBCRs also differ with estimates of 33 h for NpR6012g4[8] and 29 h for AnPixJg2.[51] All of these features were used to generate composite photocycles that are compared in Scheme 2. The discrepancies of AnPixJg2 and NpR6012g4 resolved here suggest that the structural basis of similarities and differences in photochemical behavior may not be easily inferred from sequence similarity alone, and much remains to be resolved to more fully understand the molecular basis for the differences in reaction pathways.

The overall reaction similarities are not surprising considering that AnPixJg2 and NpR6012g4 have similar static spectra (Figure 1B), 68% sequence identity (Figure S1), and similar
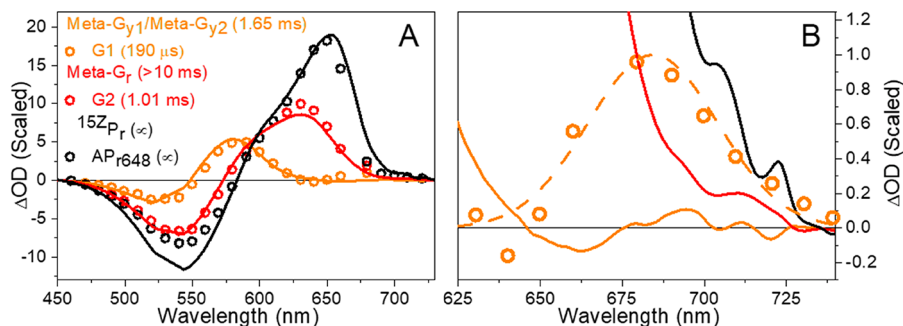

Figure 12. (A) Comparison of the extracted SADS of secondary reverse ($^{15E}P_g \rightarrow {}^{15Z}P_r$) dynamics in AnPixJg2[26] [G1, G2, and AP$_{r648}$ (empty circles)] and NpR6012g4 [Meta-G_{y1}/Meta-G_{y2}, Meta-G_r, and $^{15Z}P_r$ (solid curves)]. The respective decay constants are given in parentheses. (B) Close-up of the 625−730 nm region. The dashed orange curve represents a simple Gaussian fit to the data shown as orange empty circles and is presented as a guide to the eye. The amplitude of the data for AnPixJg2 (empty circles) was scaled to that for NpR6012g4 (solid curves) to make the amplitudes of photointermediates comparable.

Scheme 2. Photocycle of AnPixJg2[26] and NpR6012g4[21−23,30]
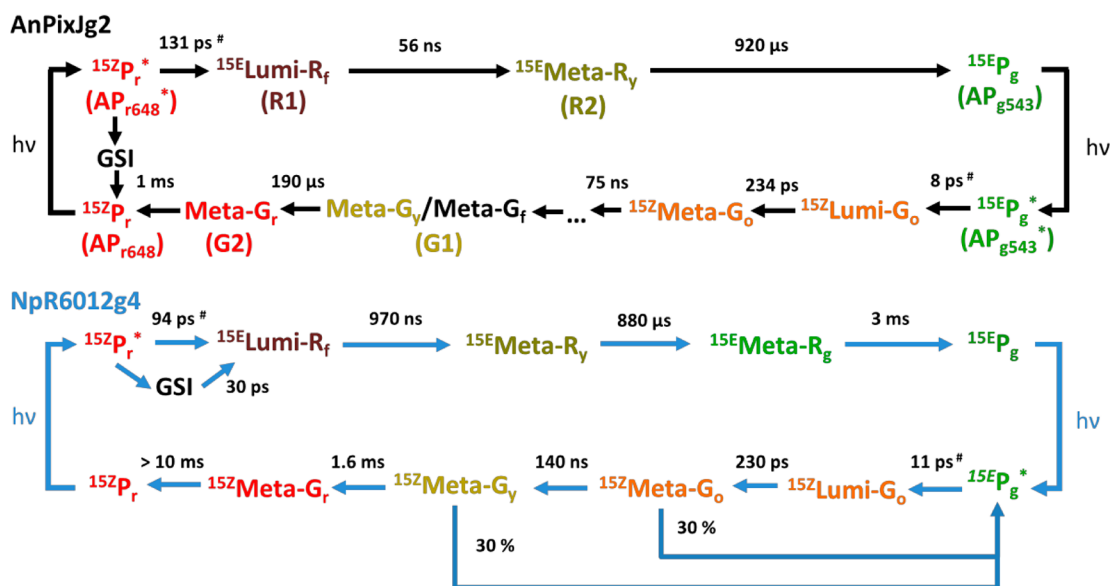
[#]Decay constants represent the weighted average of the apparent lifetimes of all excited-state P_r^* populations from Table 1 and all excited-state P_g^* populations from Table 2. The nomenclature used by Fukushima et al. for AnPixJg2[26] is shown in parentheses.

chromophore environments.[35,36,41] Thus, the possible reasons for the observed differences in the dynamics of the two proteins likely reflect smaller scale differences in the chromophore environment as further discussed below.

Forward Reaction Heterogeneity. *Assignment of Three Tyr Rotamer Populations in P_r Dark-State NpR6012g4 to the Three Excited-State Species Observed in the Forward Reaction.* The solution-phase NMR structural ensemble of NpR6012g4 P_r (6BHN) reveals that the Tyr624 side chain assumes multiple orientations. The NMR structures can be classified into three groups with a population ratio of 5:3:2 that correspond to different orientations of Tyr624 and its interactions with the bilin D-ring (Figure 13, yellow:magenta:blue). This ratio is in good agreement with an occupancy ratio of 43:33:24 of three NpR6012g4 P_r ground-state populations resolved by TA measurements (Table 1 and Figure 13), although it may be coincidental. In the largest population, the Tyr624 phenol ring is oriented perpendicular to bilin D-ring and is appressed to the C17 and C18 side chains (Figure 13C). Due to steric hindrance, this conformation would prevent the D-ring from rotating clockwise during photoisomerization, a structural assignment that best corresponds to the nonproductive GS1 (Figure 5 and Table 1). Interestingly, a similar conformation for the corresponding tyrosine was also observed in the AnPixJg2 P_r crystal structure (Protein Data Bank entry 3W2Z).

In contrast with the perpendicular orientation, the other two orientations of Tyr624 are less constricting for bilin D-ring rotation (Figure 13D,E). The upright population, where Tyr624 contacts only the C18 side chain, would cause the least steric hindrance to D-ring rotation, and for this reason, we assign this population to GS2, which has the faster evolution (Figure 13D). Tyr624 in the third population lies parallel to the D-ring and would restrict D-ring motion more strongly. We therefore assign this orientation to the GS3 population with the slower dynamics (Figure 13E). Similar Tyr orientations are likely to exist in AnPixJg2 because the $^{15Z}P_r$ dynamics of the two proteins are largely the same, although unfortunately, the structural data for Tyr rotamers are not available for AnPixJg2. It is important to
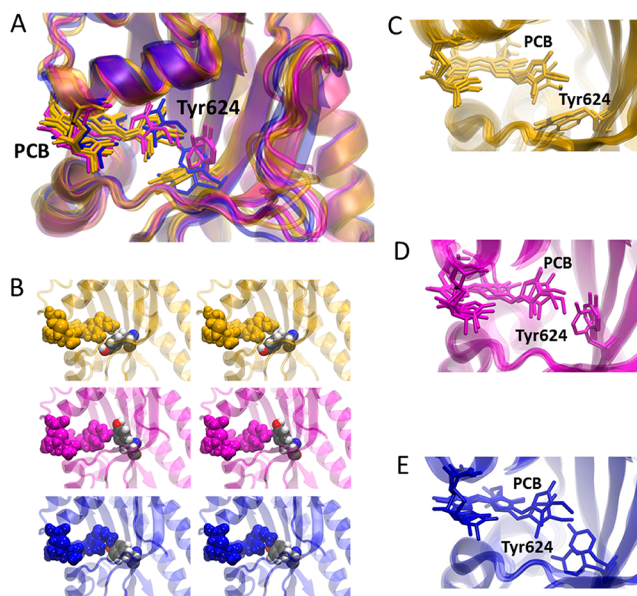

Figure 13. NMR structures of the NpR6012g4 $^{15Z}P_r$-state (Protein Data Bank entry 6BHN) chromophore pocket divided into three populations depending on the orientation of Tyr624. (A) Overlaid and (C−E) individual structures of the three populations. (B) Space-filled models of the three populations.

note that the heterogeneity of Tyr rotamer populations observed in the primary forward reaction does not extend to the secondary dynamics as sequential bi- and triphasic blue-shifting is observed for both AnPixJg2 and NpR6012g4. In these CBCRs, secondary forward P_r dynamics (of at least >1 μs dynamics) is similar, including both spectral and temporal properties, except for the penultimate Meta-R_g intermediate seen in NpR6012g4.

Hydrogen-Bonding Heterogeneity in the P_r Dark State of AnPixJg2. In addition to the Tyr rotamers, hydrogen-bonding heterogeneity has been previously suggested for the dark-adapted state of AnPixJg2.[42,52] On the basis of MD simulations, Scarbath-Evers et al.[42] proposed the existence of two $^{15Z}P_r$

substates of AnPixJg2 that differ primarily in their D-ring configurations, i.e., α-facial substate I or β-facial substate II. These substates exhibit altered hydrogen bonding networks with the protein mostly involving carbonyl and nitrogen atoms in the D-ring and the B-ring propionate. In substate I, the D-ring is more hydrogen bonded to the solvent via carbonyl to water (and Tyr352) and via nitrogen to water, whereas even the strongest hydrogen bond of the D-ring nitrogen to water is 5-fold weaker in substate II than in substate I. Hydrogen bonding between the B-ring propionate and His322 and His318 is stronger in substate II. Similar substates have not been reported in NpR6012g4[30] but likely exist. Such substates also are expected to contribute to the heterogeneity observed in NpR6012g4's forward dynamics as has been reported for other bilin-binding photoreceptors, e.g., Cph1 (Q55168) from *Synechocystis* sp. PCC6803[53] and the dark-adapted state of AnPixJg2.[42] That said, a mechanistic role of this type of structural heterogeneity on the reaction dynamic heterogeneity observed more broadly across the extended red/green (XRG) family of CBCRs[20,29−31] remains an open question.

Reverse Reaction Heterogeneity. *Shunting in NpR6012g4.* Comparison of the EADS in the secondary reverse dynamics of NpR6012g4 suggests the presence of shunts (Figure 10). Because similar shunts have been described for other bilin-binding photoreceptors, it is conceivable that these are also present in AnPixJg2.[54−56] For example, Kennis and co-workers[54] demonstrated that the secondary dynamics of bacteriophytochrome *Sa*BphP1 from the myxobacterium *Stigmatella aurantiaca* involves a 30% shunt from Lumi-R back to the P_r state ($\sim$100 ns time scale). Similarly, Hildebrandt and co-workers[55] resolved shunts in both Agp1 and Agp2, two bacteriophytochromes from *Agrobacterium fabrum*. In the forward reaction of Agp1 and the reverse reaction of Apg2, 50% and 70% of the population propagate to form the photoproduct, respectively. The presence of shunts in the secondary dynamics indicates that the primary Lumi photo-intermediate yield (Φ_p) is an upper limit approximation to the reaction yield and demonstrates the importance of studying the dynamics on both primary (femtoseconds to nanoseconds) and secondary (nanoseconds to milliseconds) time windows to obtain an accurate total reaction yield (Φ) estimate.

Far-Red Intermediate in AnPixJg2. A unique feature of the reverse dynamics of AnPixJg2 is the presence of the Meta-G_f intermediate red-shifted from the $^{15Z}P_r$ photoproduct (Figure 12B). Photointermediates red-shifted from the photoproduct absorption have been observed at later stages of the reverse reaction for NpR5113g2[31] (red/green), NpF2164g7[24] (orange/green; B2J668), and Slr1393 (P73184).[25] The presence of comparable intermediate populations in the reverse dynamics of canonical red/green CBCRs and a noncanonical orange/green CBCR suggests that this population may be more ubiquitous in the reverse pathway of CBCRs. Unfortunately, the presence or absence of this far-red-absorbing Meta-G_f intermediate cannot be easily predicted, and we currently do not have a mechanistic explanation for its production. However, comparison of decay constants for the reverse reactions of AnPixJg2 and NpR6012g4 indicates that the lifetimes of the penultimate Meta-G_y [190 μs and 1.01 ms, respectively (Figure 12A)] and Meta-G_r [1.65 and >10 ms, respectively (Figure 12A)] intermediates are significantly shorter for AnPixJg2. Hence, the presence of the far-red-absorbing Meta-G_f intermediate may be predictive of faster completion of the reverse reaction for AnPixJg2. Despite the sequence similarity between the two canonical red/green

CBCRs, much remains to be resolved to better understand the molecular basis for the differences in the observed reaction pathways.

Future Perspective. On the basis of the comparable dynamics of AnPixJg2 and NpR6012g4 reported here, substantial sequence identity of CBCRs may be useful for predicting the major steps of light-induced evolution; however, some dynamics characteristics such as time scales may vary. Studies of the secondary reverse dynamics of multiple CBCRs with substantial sequence identity may help to identify the mechanism behind the Meta-G_f population red-shifted from the $^{15Z}P_r$ photoproduct and determine if this population and intermediate shunts are unique to AnPixJg2 and NpR6012g4, respectively. Understanding the structural basis of different photochemical behavior should aid engineering efforts to improve the efficiency of the desired photochemical pathways within and between different classes of CBCRs. These and previous studies of NpR6012g4 and other red/green CBCRs provide insight into this question, contributing an overarching picture of the entire red/green family of CBCRs.

■ ASSOCIATED CONTENT

ⓈⒾ Supporting Information

The Supporting Information is available free of charge at https://pubs.acs.org/doi/10.1021/acs.biochem.0c00796.

> A discussion of the materials and methods, an amino acid sequence alignment of AnPixJg2 and NpR6012g4, comparison of AnPixJg2 and NpR6012g4 transient difference spectra and SADS, and the results of a three-population target model for AnPixJg2 (PDF)

Accession Codes

AnPixJg2, Q8YXY7; NpR6012g4, B2IU14; Slr1393, P73184; NpF2164g4, B2J668; NpF2164g5, B2J668; NpF2164g7, B2J668; RcaE, Q47897; NpF2854g3, B2IVK2; NpR1597g4, B2J0R5; NpAF142g2, B2JAQ4; NpR4776g3, B2IZ18; NpR5113g2, B2J261; Cph1, Q55168.

■ AUTHOR INFORMATION

Corresponding Author

Delmar S. Larsen − *Department of Chemistry, University of California, Davis, Davis, California 95616, United States;* Ⓞ orcid.org/0000-0003-4522-2689; Phone: +1 530-754-9075; Email: dlarsen@ucdavis.edu

Authors

Julia S. Kirpich − *Department of Chemistry, University of California, Davis, Davis, California 95616, United States*

Che-Wei Chang − *Department of Chemistry, University of California, Davis, Davis, California 95616, United States*

Jasper Franse − *Department of Chemistry, University of California, Davis, Davis, California 95616, United States*

Qinhong Yu − *Department of Chemistry, University of California, Davis, Davis, California 95616, United States*

Francisco Velazquez Escobar − *Institut für Chemie, Technische Universität Berlin, D-10623 Berlin, Germany*

Adam J. Jenkins − *Department of Chemistry, University of California, Davis, Davis, California 95616, United States*

Shelley S. Martin − *Department of Molecular and Cell Biology, University of California, Davis, Davis, California 95616, United States*

Rei Narikawa — *Department of Biological Sciences, Faculty of Sciences, Shizuoka University, Shizuoka-Shi, Shizuoka-Ken 422-8529, Japan*

James B. Ames — *Department of Chemistry, University of California, Davis, Davis, California 95616, United States*

J. Clark Lagarias — *Department of Molecular and Cell Biology, University of California, Davis, Davis, California 95616, United States;* ● orcid.org/0000-0002-2093-0403

Complete contact information is available at:
https://pubs.acs.org/10.1021/acs.biochem.0c00796

◼ ACKNOWLEDGMENTS

◼ ABBREVIATIONS

CBCR, cyanobacteriochrome; EADS, evolution-associated difference spectra; SADS, species-associated difference spectra; ESI, excited-state intermediate; ESA, excited-state absorption; SE, stimulated emission; GSB, ground-state bleach; GSA, ground-state absorbance; GAF, domain name derived from cGMP phosphodiesterase/adenylyl cyclase/FhlA; MA-MCP, methyl-accepting chemotaxis protein output domain; HAMP, domain name derived from histidine kinases, adenylate cyclases, methyl-accepting proteins, and phosphatases; NOPA, noncollinear optical parametric amplifier; PCB, phycocyanobilin; $^{15Z}P_r$, red-absorbing dark-adapted state of red/green CBCRs; $^{15E}P_g$, green-absorbing photoproduct state of red/green CBCRs; P_r^* (P_g^*), excited-state population(s) derived from photoexcitation of $^{15Z}P_r$ ($^{15E}P_g$); Lumi-R$_f$, primary photointermediate derived from the $^{15Z}P_r$ parental state that absorbs in the far-red region; Lumi-G$_o$, primary photointermediate derived from the $^{15E}P_g$ parental state that absorbs in the orange region; Meta$_x$, photointermediates following primary intermediate Lumi, where the subscript x indicates the letter of the color of the absorption spectrum (r for red, g for green, o for orange, f for far-red, b for blue, and y for yellow)[1]; Φ, overall photocycle quantum yield; Φ$_b$, branching yield; Φ$_p$ (Lumi-R$_f$/Lumi-G$_o$), quantum yield of the primary intermediate Lumi-R$_f$/Lumi-G$_o$.

◼ REFERENCES

(1) Gottlieb, S. M., Kim, P. W., Corley, S. C., Madsen, D., Hanke, S. J., Chang, C.-W., Rockwell, N. C., Martin, S. S., Lagarias, J. C., and Larsen, D. S. (2014) Primary and Secondary Photodynamics of the Violet/Orange Dual-Cysteine NpF2164g3 Cyanobacteriochrome Domain from Nostoc punctiforme. *Biochemistry 53*, 1029−1040.

(2) Smith, H. (1994) Sensing the light environment: the functions of the phytochrome family. In *Photomorphogenesis in Plants* (Kendrick, R. E., and Kronenberg, G. H. M., Eds.) pp 377−416, Springer, Dordrecht, The Netherlands.

(3) Rockwell, N. C., Martin, S. S., Gulevich, A. G., and Lagarias, J. C. (2012) Phycoviolobilin formation and spectral tuning in the DXCF cyanobacteriochrome subfamily. *Biochemistry 51*, 1449−1463.

(4) Fushimi, K., Ikeuchi, M., and Narikawa, R. (2017) The expanded red/green cyanobacteriochrome lineage: An evolutionary hot spot. *Photochem. Photobiol. 93* (3), 903−906.

(5) Fushimi, K., and Narikawa, R. (2019) Cyanobacteriochromes: photoreceptors covering the entire UV-to-visible spectrum. *Curr. Opin. Struct. Biol. 57*, 39−46.

(6) Ikeuchi, M., and Ishizuka, T. (2008) Cyanobacteriochromes: a new superfamily of tetrapyrrole-binding photoreceptors in cyanobacteria. *Photochem. Photobiol. Sci. 7*, 1159−1167.

(7) Rockwell, N. C., Martin, S. S., Feoktistova, K., and Lagarias, J. C. (2011) Diverse two-cysteine photocycles in phytochromes and cyanobacteriochromes. *Proc. Natl. Acad. Sci. U. S. A. 108*, 11854−11859.

(8) Rockwell, N. C., Martin, S. S., and Lagarias, J. C. (2012) Red/Green Cyanobacteriochromes: Sensors of Color and Power. *Biochemistry 51*, 9667−9677.

(9) Rockwell, N. C., Martin, S. S., and Lagarias, J. C. (2012) Mechanistic Insight into the Photosensory Versatility of DXCF Cyanobacteriochromes. *Biochemistry 51*, 3576−3585.

(10) Rockwell, N. C., Martin, S. S., and Lagarias, J. C. (2016) Identification of Cyanobacteriochromes Detecting Far-Red Light. *Biochemistry 55*, 3907−3919.

(11) Pennacchietti, F., Losi, A., Xu, X. L., Zhao, K. H., Gartner, W., Viappiani, C., Cella, F., Diaspro, A., and Abbruzzetti, S. (2015) Photochromic conversion in a red/green cyanobacteriochrome from Synechocystis PCC6803: quantum yields in solution and photoswitching dynamics in living E. coli cells. *Photochemical & photobiological sciences: Official journal of the European Photochemistry Association and the European Society for Photobiology 14*, 229−237.

(12) Gottlieb, S. M., Kim, P. W., Rockwell, N. C., Hirose, Y., Ikeuchi, M., Lagarias, J. C., and Larsen, D. S. (2013) Primary photodynamics of the green/red-absorbing photoswitching regulator of the chromatic adaptation E domain from Fremyella diplosiphon. *Biochemistry 52*, 8198−8208.

(13) Chang, C.-W., Gottlieb, S. M., Rockwell, N. C., Martin, S. S., Lagarias, J. C., and Larsen, D. S. (2016) Tracking the secondary photodynamics of the green/red cyanobacteriochrome RcaE from Fremyella diplosiphon. *Chem. Phys. Lett. 644*, 225−230.

(14) Hirose, Y., Rockwell, N. C., Nishiyama, K., Narikawa, R., Ukaji, Y., Inomata, K., Lagarias, J. C., and Ikeuchi, M. (2013) Green/red cyanobacteriochromes regulate complementary chromatic acclimation via a protochromic photocycle. *Proc. Natl. Acad. Sci. U. S. A. 110*, 4974−4979.

(15) Narikawa, R., Nakajima, T., Aono, Y., Fushimi, K., Enomoto, G., Win, N., Itoh, S., Sato, M., and Ikeuchi, M. (2015) A biliverdin-binding cyanobacteriochrome from the chlorophyll d−bearing cyanobacterium Acaryochloris marina. *Sci. Rep. 5*, 7950.

(16) Narikawa, R., Fushimi, K., Win, N., and Ikeuchi, M. (2015) Red-shifted red/green-type cyanobacteriochrome AM1_1870g3 from the chlorophyll d-bearing cyanobacterium Acaryochloris marina. *Biochem. Biophys. Res. Commun. 461*, 390−395.

(17) Fushimi, K., Nakajima, T., Aono, Y., Yamamoto, T., Win, N., Ikeuchi, M., Sato, M., and Narikawa, R. (2016) Photoconversion and Fluorescence Properties of a Red/Green-Type Cyanobacteriochrome AM1_C0023g2 That Binds Not Only Phycocyanobilin But Also Biliverdin. *Front. Microbiol. 7*, 588.

(18) Loughlin, P. C., Duxbury, Z., Mugerwa, T. T. M., Smith, P. M. C., Willows, R. D., and Chen, M. (2016) Spectral properties of bacteriophytochrome AM1_5894 in the chlorophyll d-containing cyanobacterium Acaryochloris marina. *Sci. Rep. 6*, 27547.

(19) Blain-Hartung, M., Rockwell, N. C., Moreno, M. V., Martin, S. S., Gan, F., Bryant, D. A., and Lagarias, J. C. (2018) Cyanobacteriochrome-based photoswitchable adenylyl cyclases (cPACs) for broad spectrum light regulation of cAMP levels in cells. *J. Biol. Chem. 293*, 8473−8483.

(20) Gottlieb, S. M., Kim, P. W., Chang, C.-W., Hanke, S. J., Hayer, R. J., Rockwell, N. C., Martin, S. S., Lagarias, J. C., and Larsen, D. S. (2015)

Conservation and Diversity in the Primary Forward Photodynamics of Red/Green Cyanobacteriochromes. *Biochemistry 54*, 1028−1042.

(21) Kim, P. W., Freer, L. H., Rockwell, N. C., Martin, S. S., Lagarias, J. C., and Larsen, D. S. (2012) Femtosecond Photodynamics of the Red/Green Cyanobacteriochrome NpR6012g4 from Nostoc punctiforme. 1. Forward Dynamics. *Biochemistry 51*, 608−618.

(22) Kim, P. W., Freer, L. H., Rockwell, N. C., Martin, S. S., Lagarias, J. C., and Larsen, D. S. (2012) Femtosecond Photodynamics of the Red/Green Cyanobacteriochrome NpR6012g4 from Nostoc punctiforme. 2. Reverse Dynamics. *Biochemistry 51*, 619−630.

(23) Kim, P. W., Freer, L. H., Rockwell, N. C., Martin, S. S., Lagarias, J. C., and Larsen, D. S. (2012) Second-Chance Forward Isomerization Dynamics of the Red/Green Cyanobacteriochrome NpR6012g4 from Nostoc punctiforme. *J. Am. Chem. Soc. 134*, 130−133.

(24) Kirpich, J. S., Chang, C.-W., Madsen, D., Gottlieb, S. M., Martin, S. S., Rockwell, N. C., Lagarias, J. C., and Larsen, D. S. (2018) Noncanonical Photodynamics of the Orange/Green Cyanobacteriochrome Power Sensor NpF2164g7 from the PtxD Phototaxis Regulator of Nostoc punctiforme. *Biochemistry 57*, 2636−2648.

(25) Slavov, C., Xu, X., Zhao, K.-h., Gärtner, W., and Wachtveitl, J. (2015) Detailed insight into the ultrafast photoconversion of the cyanobacteriochrome Slr1393 from Synechocystis sp. *Biochim. Biophys. Acta, Bioenerg. 1847*, 1335−1344.

(26) Fukushima, Y., Iwaki, M., Narikawa, R., Ikeuchi, M., Tomita, Y., and Itoh, S. (2011) Photoconversion Mechanism of a Green/Red Photosensory Cyanobacteriochrome AnPixJ: Time-Resolved Optical Spectroscopy and FTIR Analysis of the AnPixJ-GAF2 Domain. *Biochemistry 50*, 6328−6339.

(27) Narikawa, R., Fukushima, Y., Ishizuka, T., Itoh, S., and Ikeuchi, M. (2008) A novel photoactive GAF domain of cyanobacteriochrome AnPixJ that shows reversible green/red photoconversion. *J. Mol. Biol. 380*, 844−855.

(28) Xu, X. L., Gutt, A., Mechelke, J., Raffelberg, S., Tang, K., Miao, D., Valle, L., Borsarelli, C. D., Zhao, K. H., and Gartner, W. (2014) Combined mutagenesis and kinetics characterization of the bilin-binding GAF domain of the protein Slr1393 from the Cyanobacterium Synechocystis PCC6803. *ChemBioChem 15*, 1190−1199.

(29) Jenkins, A. J., Gottlieb, S. M., Chang, C.-W., Hayer, R. J., Martin, S. S., Lagarias, J. C., and Larsen, D. S. (2019) Conservation and diversity in the secondary forward photodynamics of red/green cyanobacteriochromes. *Photochem. Photobiol. Sci. 18*, 2539−2552.

(30) Lim, S., Yu, Q., Gottlieb, S. M., Chang, C.-W., Rockwell, N. C., Martin, S. S., Madsen, D., Lagarias, J. C., Larsen, D. S., and Ames, J. B. (2018) Correlating structural and photochemical heterogeneity in cyanobacteriochrome NpR6012g4. *Proc. Natl. Acad. Sci. U. S. A. 115*, 4387−4392.

(31) Jenkins, A. J., Gottlieb, S. M., Chang, C.-W., Kim, P. W., Hayer, R. J., Hanke, S. J., Martin, S. S., Lagarias, J. C., and Larsen, D. S. (2020) Conservation and Diversity in the Primary Reverse Photodynamics of Red/Green Cyanobacteriochromes. *Biochemistry 59*, 4015−4028.

(32) Rockwell, N. C., Martin, S. S., Gulevich, A. G., and Lagarias, J. C. (2014) Conserved phenylalanine residues are required for blue-shifting of cyanobacteriochrome photoproducts. *Biochemistry 53*, 3118−3130.

(33) Rockwell, N. C., Martin, S. S., Gan, F., Bryant, D. A., and Lagarias, J. C. (2015) NpR3784 is the prototype for a distinctive group of red/green cyanobacteriochromes using alternative Phe residues for photoproduct tuning. *Photochem. Photobiol. Sci. 14*, 258−269.

(34) Chang, C.-W., Gottlieb, S. M., Kim, P. W., Rockwell, N. C., Lagarias, J. C. L., and Larsen, D. S. (2013) Reactive Ground-State Pathways Are Not Ubiquitous in Red/Green Cyanobacteriochromes. *J. Phys. Chem. B 117*, 11229−11238.

(35) Rockwell, N. C., Martin, S. S., Lim, S., Lagarias, J. C., and Ames, J. B. (2015) Characterization of Red/Green Cyanobacteriochrome NpR6012g4 by Solution Nuclear Magnetic Resonance Spectroscopy: A Protonated Bilin Ring System in Both Photostates. *Biochemistry 54*, 2581−2600.

(36) Rockwell, N. C., Martin, S. S., Lim, S., Lagarias, J. C., and Ames, J. B. (2015) Characterization of Red/Green Cyanobacteriochrome NpR6012g4 by Solution Nuclear Magnetic Resonance Spectroscopy:

A Hydrophobic Pocket for the C15-E,anti Chromophore in the Photoproduct. *Biochemistry 54*, 3772−3783.

(37) Velazquez Escobar, F., Utesch, T., Narikawa, R., Ikeuchi, M., Mroginski, M. A., Gärtner, W., and Hildebrandt, P. (2013) Photoconversion Mechanism of the Second GAF Domain of Cyanobacteriochrome AnPixJ and the Cofactor Structure of Its Green-Absorbing State. *Biochemistry 52*, 4871−4880.

(38) Song, C., Velazquez Escobar, F., Xu, X.-L., Narikawa, R., Ikeuchi, M., Siebert, F., Gärtner, W., Matysik, J., and Hildebrandt, P. (2015) A Red/Green Cyanobacteriochrome Sustains Its Color Despite a Change in the Bilin Chromophore's Protonation State. *Biochemistry 54*, 5839−5848.

(39) Narikawa, R., Muraki, N., Shiba, T., Ikeuchi, M., and Kurisu, G. (2009) Crystallization and preliminary X-ray studies of the chromophore-binding domain of cyanobacteriochrome AnPixJ from Anabaena sp. PCC 7120. *Acta Crystallogr., Sect. F: Struct. Biol. Cryst. Commun. 65*, 159−162.

(40) Narikawa, R., Ishizuka, T., Muraki, N., Shiba, T., Kurisu, G., and Ikeuchi, M. (2013) Structures of cyanobacteriochromes from phototaxis regulators AnPixJ and TePixJ reveal general and specific photoconversion mechanism. *Proc. Natl. Acad. Sci. U. S. A. 110*, 918−923.

(41) Song, C., Narikawa, R., Ikeuchi, M., Gärtner, W., and Matysik, J. (2015) Color Tuning in Red/Green Cyanobacteriochrome AnPixJ: Photoisomerization at C15 Causes an Excited-State Destabilization. *J. Phys. Chem. B 119*, 9688−9695.

(42) Scarbath-Evers, L. K., Jahnigen, S., Elgabarty, H., Song, C., Narikawa, R., Matysik, J., and Sebastiani, D. (2017) Structural heterogeneity in a parent ground-state structure of AnPixJg2 revealed by theory and spectroscopy. *Phys. Chem. Chem. Phys. 19*, 13882−13894.

(43) Rockwell, N. C., Shang, L., Martin, S. S., and Lagarias, J. C. (2009) Distinct classes of red/far-red photochemistry within the phytochrome superfamily. *Proc. Natl. Acad. Sci. U. S. A. 106*, 6123−6127.

(44) Carroll, E. C., Compton, O. C., Madsen, D., Osterloh, F. E., and Larsen, D. S. (2008) Ultrafast carrier dynamics in exfoliated and functionalized calcium niobate nanosheets in water and methanol. *J. Phys. Chem. C 112*, 2394−2403.

(45) Gottlieb, S. M., Corley, S. C., Madsen, D., and Larsen, D. S. (2012) Note: A flexible light emitting diode-based broadband transient-absorption spectrometer. *Rev. Sci. Instrum. 83*, 056107.

(46) van Stokkum, I. H. M., Larsen, D. S., and van Grondelle, R. (2004) Global and target analysis of time-resolved spectra. *Biochim. Biophys. Acta, Bioenerg. 1657*, 82−104.

(47) Holzwarth, A. R. (1996) Data Analysis of Time-Resolved Measurements. In *Biophysical techniques in photosynthesis* (Amesz, J., and Hoff, A. J., Eds.) pp 75−92, Springer, Dordrecht, The Netherlands.

(48) Stojković, E. A., Toh, K. C., Alexandre, M. T. A., Baclayon, M., Moffat, K., and Kennis, J. T. M. (2014) FTIR Spectroscopy Revealing Light-Dependent Refolding of the Conserved Tongue Region of Bacteriophytochrome. *J. Phys. Chem. Lett. 5*, 2512−2515.

(49) Velázquez Escobar, F., Buhrke, D., Michael, N., Sauthof, L., Wilkening, S., Tavraz, N. N., Salewski, J., Frankenberg-Dinkel, N., Mroginski, M. A., Scheerer, P., Friedrich, T., Siebert, F., and Hildebrandt, P. (2017) Common Structural Elements in the Chromophore Binding Pocket of the Pfr State of Bathy Phytochromes. *Photochem. Photobiol. 93*, 724−732.

(50) Vardeny, Z., and Tauc, J. (1981) Picosecond coherence coupling in the pump and probe technique. *Opt. Commun. 39*, 396−400.

(51) Fushimi, K., Enomoto, G., Ikeuchi, M., and Narikawa, R. (2017) Distinctive Properties of Dark Reversion Kinetics between Two Red/Green-Type Cyanobacteriochromes and their Application in the Photoregulation of cAMP Synthesis. *Photochem. Photobiol. 93*, 681−691.

(52) Rao, A. G., Wiebeler, C., Sen, S., Cerutti, D. S., and Schapiro, I. (2020) Histidine Protonation Controls Structural Heterogeneity in the Cyanobacteriochrome AnPixJg2. *bioRxiv*, DOI: 10.1101/2020.08.21.260158.

(53) Kirpich, J. S., Mix, L. T., Martin, S. S., Rockwell, N. C., Lagarias, J. C., and Larsen, D. S. (2018) Protonation Heterogeneity Modulates the Ultrafast Photocycle Initiation Dynamics of Phytochrome Cph1. *J. Phys. Chem. Lett. 9*, 3454−3462.

(54) Mathes, T., Ravensbergen, J., Kloz, M., Gleichmann, T., Gallagher, K. D., Woitowich, N. C., St. Peter, R., Kovaleva, S. E., Stojković, E. A., and Kennis, J. T. M. (2015) Femto- to Microsecond Photodynamics of an Unusual Bacteriophytochrome. *J. Phys. Chem. Lett. 6*, 239−243.

(55) Buhrke, D., Kuhlmann, U., Michael, N., and Hildebrandt, P. (2018) The Photoconversion of Phytochrome Includes an Unproductive Shunt Reaction Pathway. *ChemPhysChem 19*, 566−570.

(56) Zienicke, B., Molina, I., Glenz, R., Singer, P., Ehmer, D., Escobar, F. V., Hildebrandt, P., Diller, R., and Lamparter, T. (2013) Unusual Spectral Properties of Bacteriophytochrome Agp2 Result from a Deprotonation of the Chromophore in the Red-absorbing Form Pr. *J. Biol. Chem. 288*, 31738−31751.